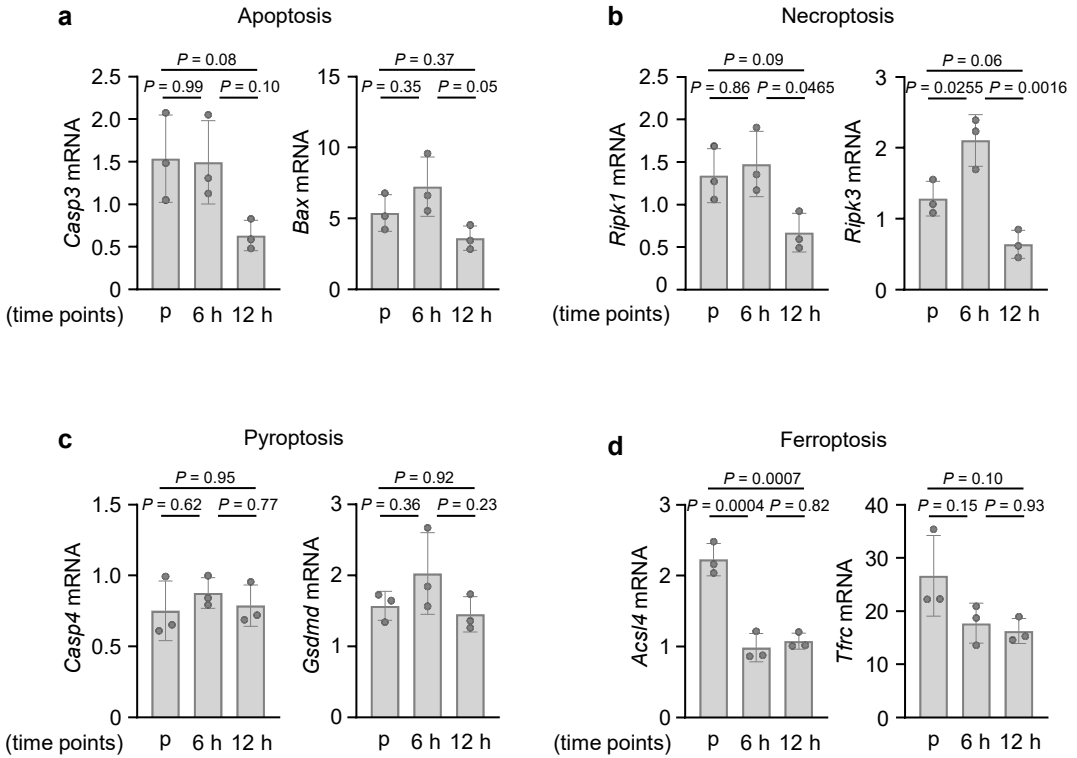
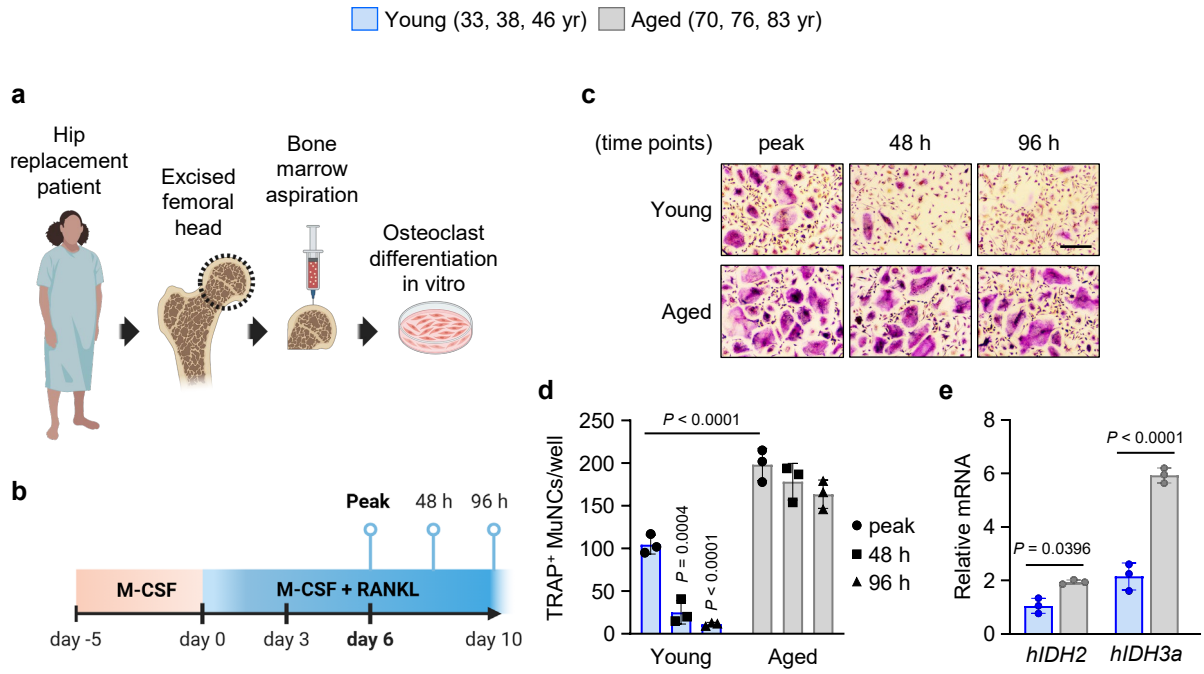
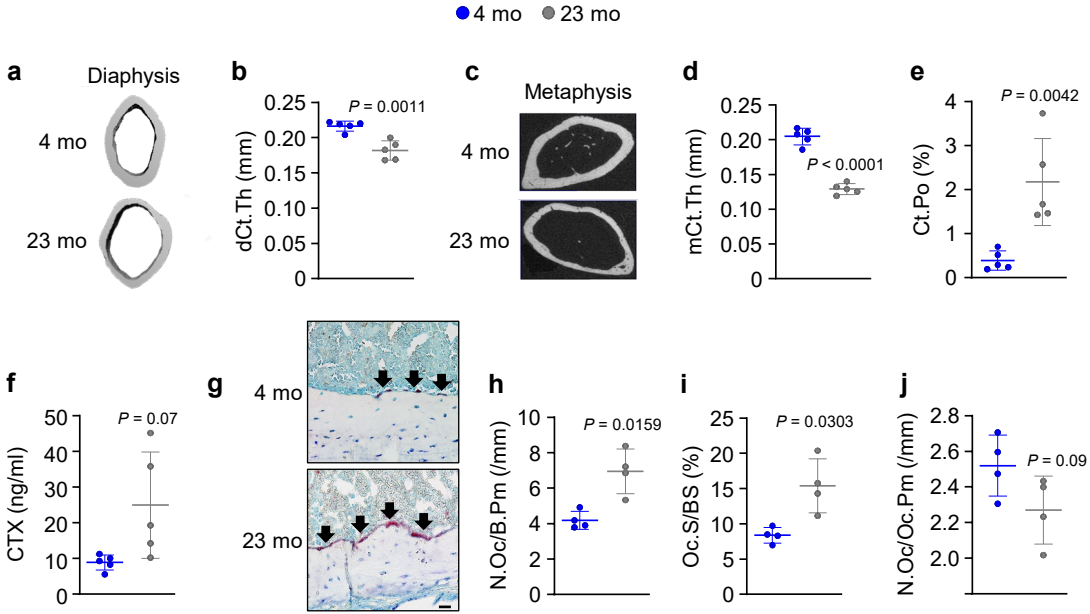


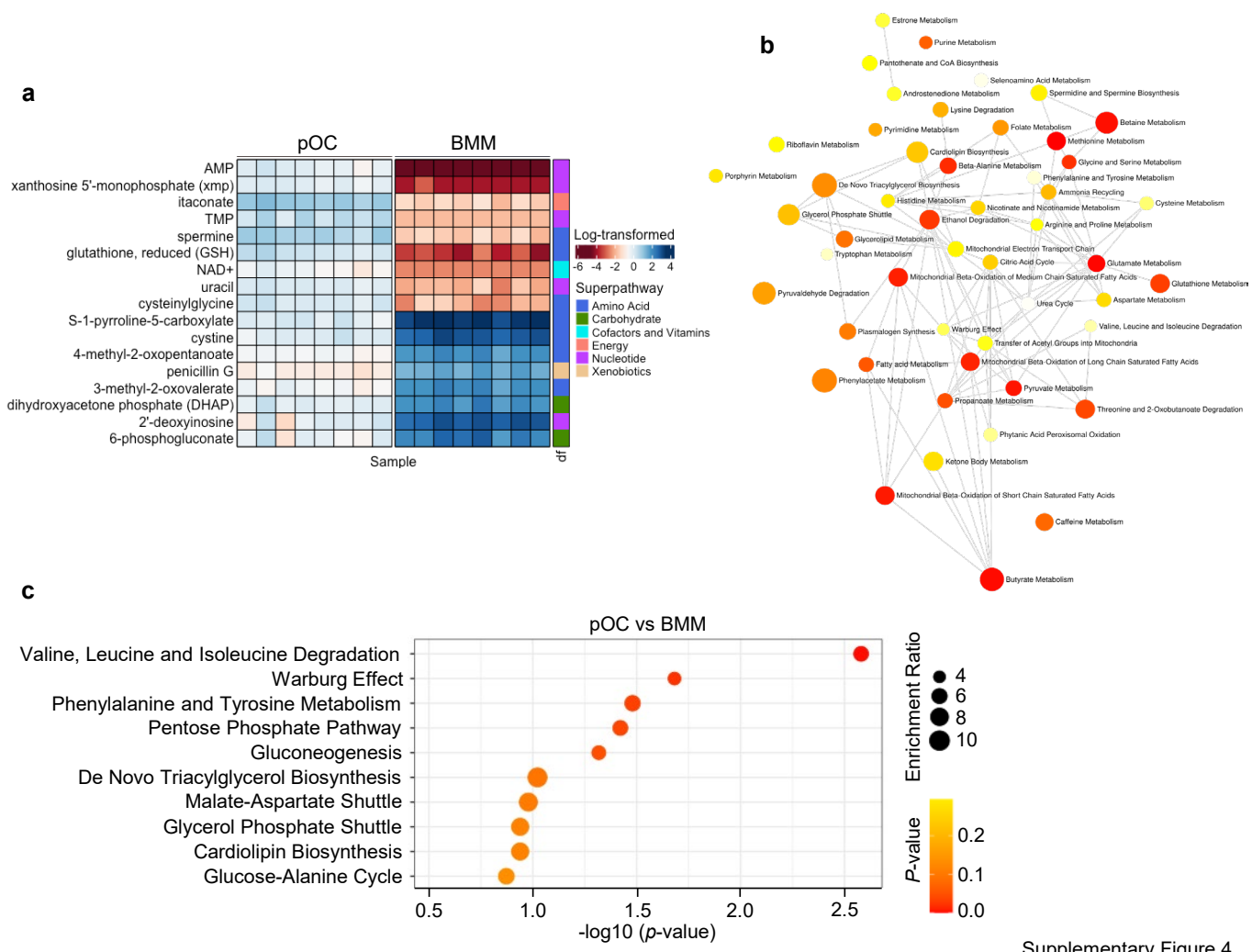
Supplementary Figure 1



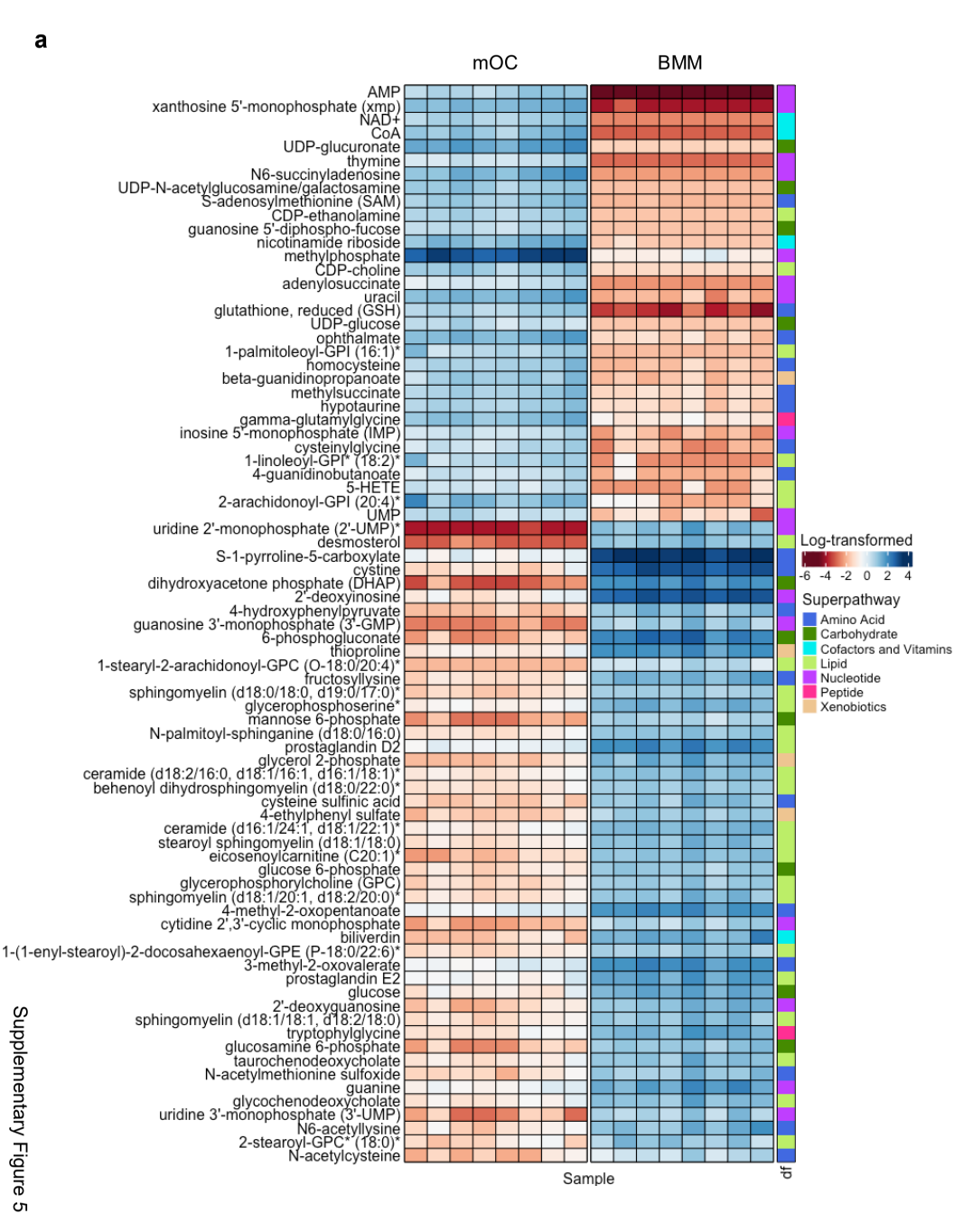
Supplementary Figure 2



Supplementary Figure 3

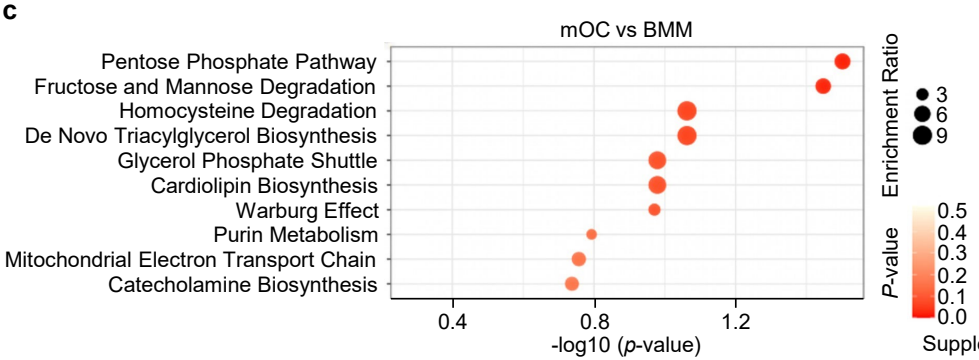


Supplementary Figure 4



Supplementary Figure 5



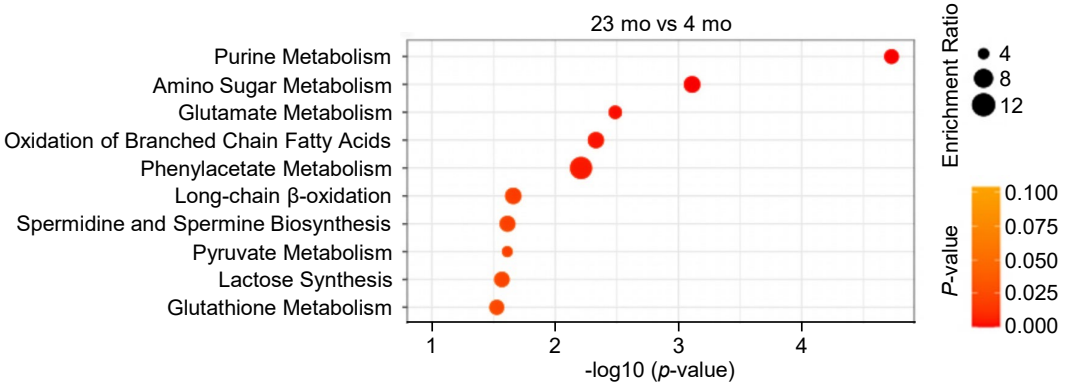


Supplementary Figure 5_continued

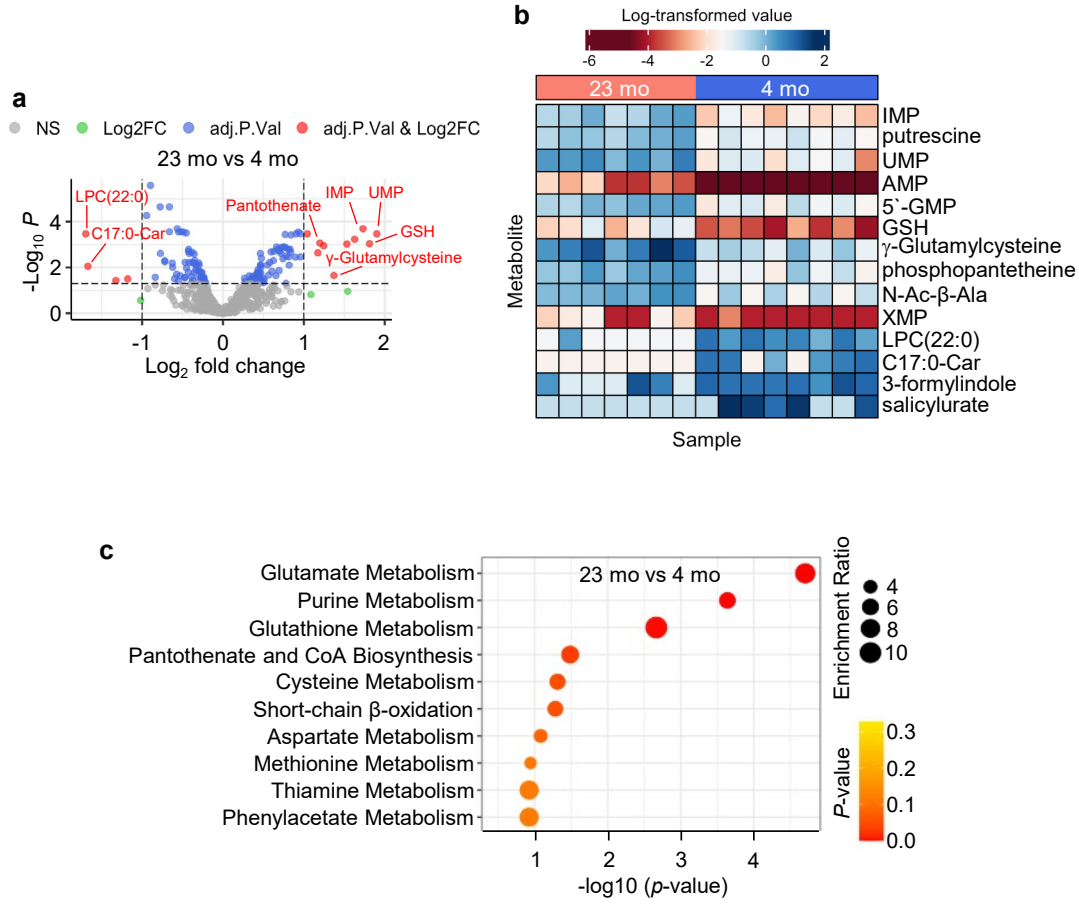
a

GO ID	GO description	Input compounds	Overlap	P value	FDR
GO:0006107	Oxaloacetate metabolic process	8	4	9.75×10^{-5}	0.044

b



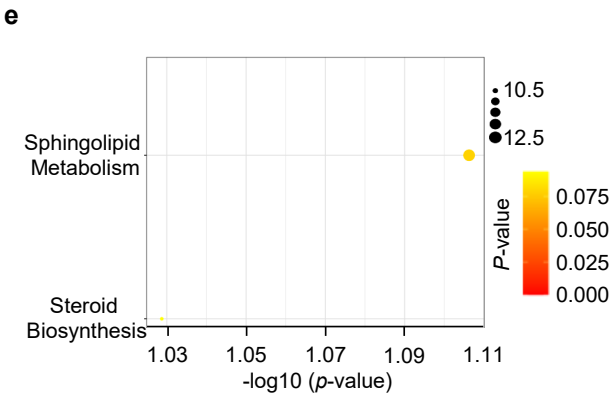
Supplementary Figure 6



Supplementary Figure 7

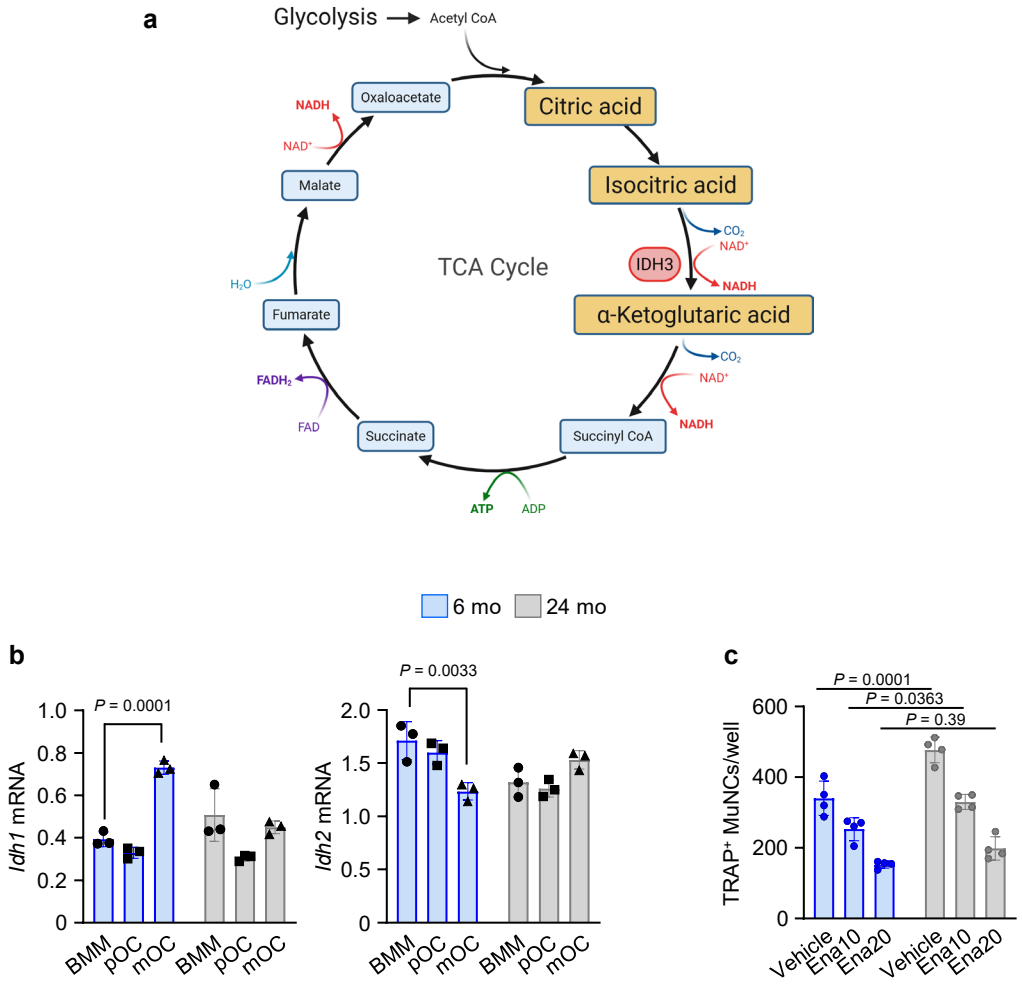


Supplementary Figure 7_continued_1

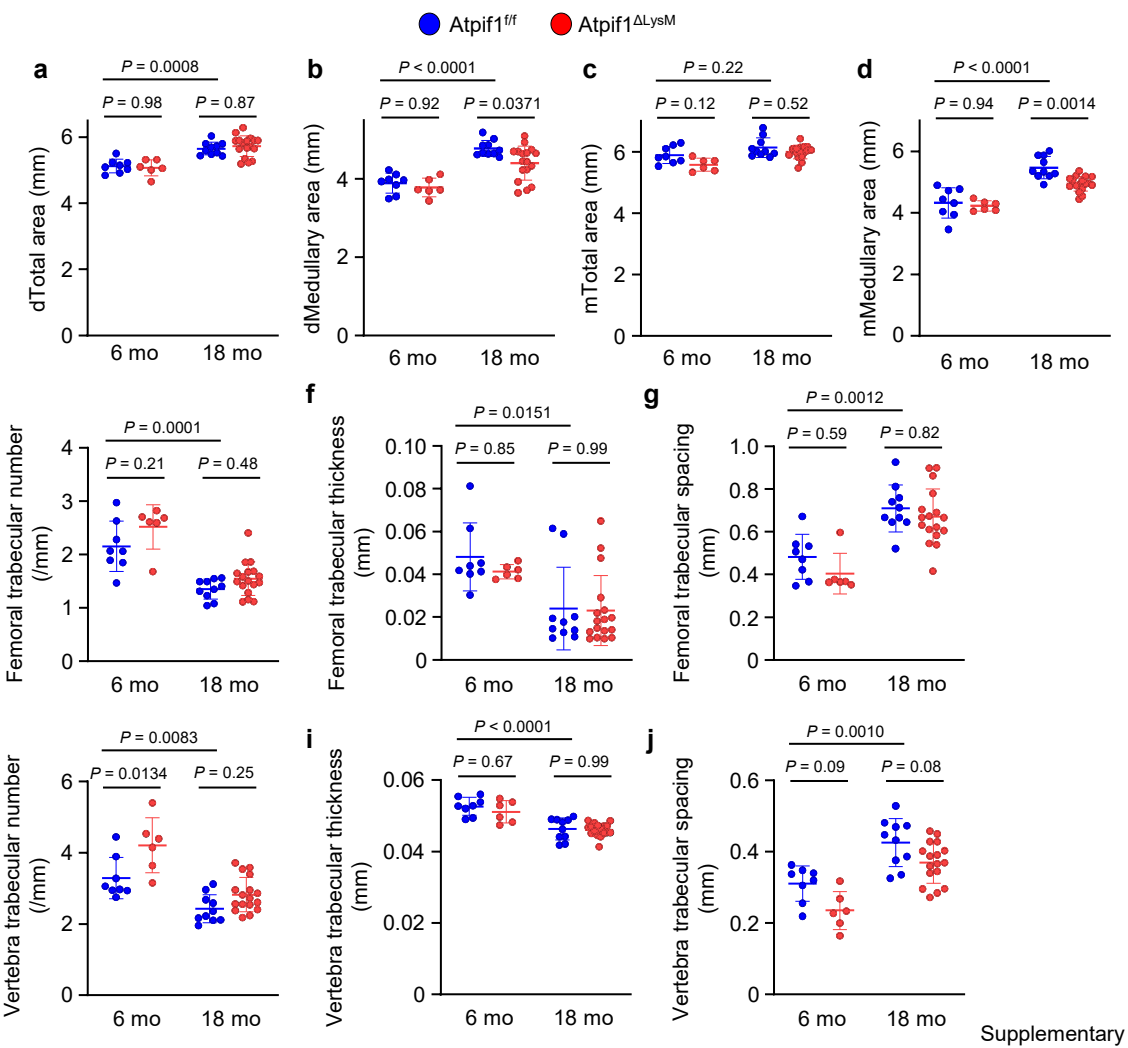




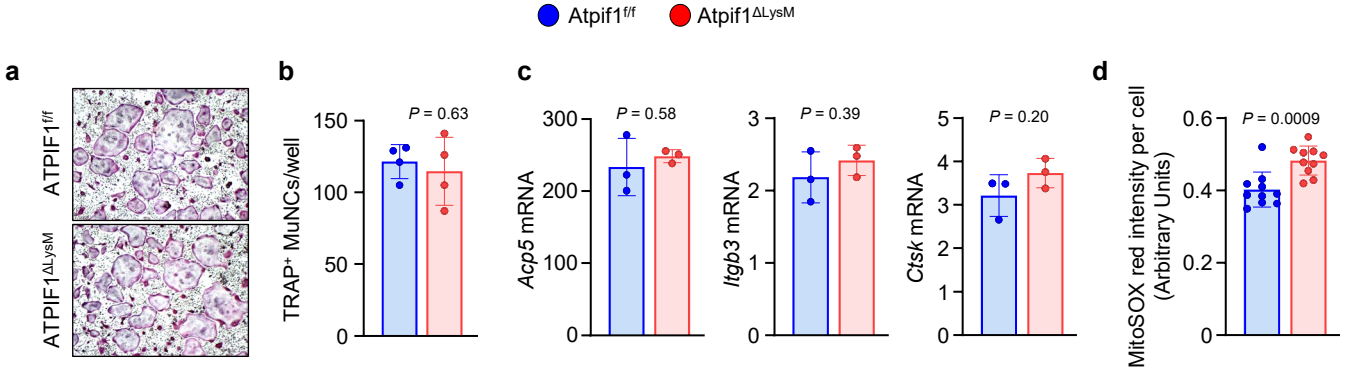
Supplementary Figure 7_continued_2



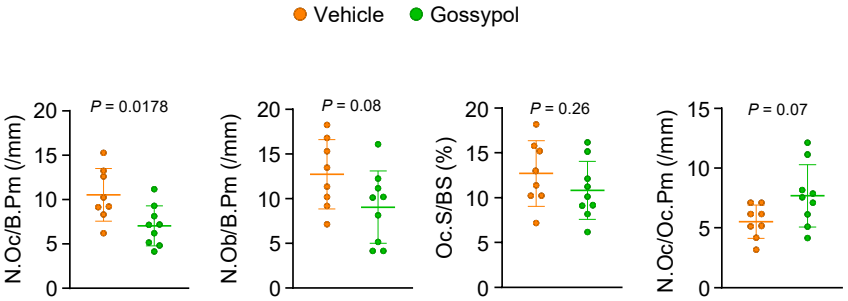
Supplementary Figure 8



Supplementary Figure 9



Supplementary Figure 10



Supplementary Figure 11

SUPPLEMENTARY FIGURE LEGENDS

Supplementary Fig. 1. Time-dependent changes in cell death pathway-related gene expression after peak osteoclast formation. (**a–d**) Relative mRNA expression of genes associated with apoptosis (**a**), necroptosis (**b**), pyroptosis (**c**), and ferroptosis (**d**) in osteoclast cultures from aged mice at peak formation and 6 h or 12 h thereafter. Data are means ± s.d. Statistical analyses were performed using one-way ANOVA. Exact *P* values are shown in the panels. All measures were performed in cultured BMMs pooled from 4–5 mice/group.

Supplementary Fig. 2. Human osteoclast cultures from young and aged donors. (**a**) Schematic of human osteoclast generation from femoral heads obtained during hip replacement surgery. Bone marrow cells were aspirated from excised femoral heads and differentiated *in vitro* into osteoclasts. (**b**) Experimental scheme for *in vitro* osteoclast differentiation and post-maturation analysis. (**c, d**) Representative TRAP staining images (**c**) and quantification of TRAP-positive multinucleated cells (MuNCs) per well (**d**) in osteoclast cultures generated from young (39.0 ± 6.6 years) and aged human donors (76.3 ± 6.5 years) at peak formation and 48 h or 96 h thereafter. (**e**) Relative mRNA expression of hIDH2 and hIDH3a in osteoclast cultures from young and aged human donors. Data are means ± s.d. Statistical analyses were performed using unpaired two-tailed Student's t-test or two-way ANOVA, as appropriate. Exact *P* values are shown in the panels. Scale bars, 500 μm. All measures were performed in cultured BMMs pooled from 3 donors/group.

Supplementary Fig. 3. *In vivo* and histomorphometric analyses of aged bones. (**a–e**) Representative cross-sectional micro-CT images and quantification of cortical parameters in 4- and 23-month-old female mice (n = 5 animals/group). (**a, b**) Diaphyseal cortical images (**a**) and

cortical thickness at the femoral diaphysis (dCt.Th; **b**). (**c, d**) Metaphyseal cortical images (**c**) and cortical thickness at the femoral metaphysis (mCt.Th; **d**). (**e**,) Cortical porosity (Ct.Po). (**f**) Serum CTX levels in 4- and 23-month-old female mice. (**g–j**) Histomorphometric analyses of the femoral endocortical surface in 4- and 23-month-old female mice. (**g**) Representative images used for osteoclast number and size assessment. Scale bars, 100 μm. (**h**) Number of osteoclasts per bone perimeter (N.Oc/B.Pm). (**i**) Osteoclast surface per bone surface (Oc.S/BS). (**j**) Osteoclast number relative to osteoclast perimeter (N.Oc/Oc.Pm). Data are means ± s.d. Statistical analyses were performed using an unpaired two-tailed Student's t-test. Exact *P* values are shown in the panels.

Supplementary Fig. 4. Metabolomic analyses of pOCs relative to BMMs during osteoclast differentiation. (**a–c**) Additional metabolomic analyses of pOCs relative to BMMs, including a heat map of selected metabolites (**a**), network analysis (**b**), and pathway-enrichment analysis (**c**). In (**c**), dot size indicates enrichment ratio, and colour indicates *P* value. Criteria for differential metabolite abundance and pathway-enrichment analysis are described in the Methods. All measures were performed in cultured BMMs pooled from 4–5 mice/group.

Supplementary Fig. 5. Metabolomic analyses of mOCs relative to BMMs during osteoclast differentiation. (**a–c**) Additional metabolomic analyses of mOCs relative to BMMs, including a heat map of selected metabolites (**a**), network analysis (**b**), and pathway-enrichment analysis (**c**). In (**c**) dot size indicates enrichment ratio, and colour indicates *P* value. Criteria for differential metabolite abundance and pathway-enrichment analysis are described in the Methods. All measures were performed in cultured BMMs pooled from 4–5 mice/group.

Supplementary Fig. 6. Enrichment analyses of mOCs during skeletal aging. (**a, b**) Enrichment analyses of metabolites altered in mOCs from 23-month-old relative to 4-month-old female mice, including GO enrichment analysis of metabolites increased in aged mOCs (**a**) and pathway-enrichment analysis of metabolites decreased in aged mOCs (**b**). In (**a**) the table shows the GO identifier, GO description, number of input compounds, overlap, raw P value, and false discovery rate (FDR)-adjusted P value. In (**b**) dot size indicates enrichment ratio, and colour indicates P value. Criteria for differential metabolite abundance and enrichment analyses are described in the Methods. All measures were performed in cultured BMMs pooled from 4–5 mice/group.

Supplementary Fig. 7. Metabolomic profiling of BMMs during skeletal aging. (**a–d**) Metabolomic analyses of BMMs from 23-month-old relative to 4-month-old female mice, including a volcano plot of differentially abundant metabolites (**a**), a heat map of selected metabolites (**b**), pathway-enrichment analysis (**c**), and network analysis (**d**) of metabolites increased in aged BMMs. (**e, f**) Pathway-enrichment analysis (**e**) and network analysis (**f**) of metabolites decreased in BMMs from 23-month-old relative to 4-month-old female mice. In (**c, e**) dot size indicates enrichment ratio, and colour indicates *P* value. Criteria for differential metabolite abundance and pathway-enrichment analysis are described in the Methods. All measures were performed in cultured BMMs pooled from 4–5 mice/group.

Supplementary Fig. 8. Age-associated metabolic remodeling in osteoclasts is not accompanied by induction of Idh1 or Idh2. (**a**) Schematic of the tricarboxylic acid cycle, highlighting citrate, isocitrate, α-ketoglutarate, and the step catalysed by IDH3. (**b**) Relative mRNA expression of *Idh1* and *Idh2* in BMMs, pOCs, and mOCs from 6- and 24-month-old female

mice. (**c** Quantification of TRAP-positive multinucleated cells (MuNCs) per well in osteoclast cultures from 6- and 24-month-old female mice treated with vehicle or enasidenib at the indicated concentrations (μM). Data are means ± s.d. Statistical analyses were performed using two-way ANOVA, as appropriate. Exact *P* values are shown in the panels. All measures were performed in cultured BMMs pooled from 4–5 mice/group.

Supplementary Fig. 9. Additional cortical and trabecular morphometric analyses of control and *Atpif1*$^{\Delta LysM}$ mice. (**a–d**) Micro-CT–based quantification of femoral cortical parameters in control and *Atpif1*$^{\Delta LysM}$ mice at 6 and 18 months of age (n = 6–17 animals/group). (**a**) Total area at the femoral diaphysis (dTotal area). (**b**) Medullary area at the femoral diaphysis (dMedullary area). (**c**) Total area at the femoral metaphysis (mTotal area). (**d**) Medullary area at the femoral metaphysis (mMedullary area). (**e–g**) Micro-CT–based quantification of femoral trabecular parameters in control and *Atpif1*$^{\Delta LysM}$ mice at 6 and 18 months of age (n = 6–17 animals/group). (**e**) Femoral trabecular number. (**f**) Femoral trabecular thickness. (**g**) Femoral trabecular spacing. (**h–j**) Micro-CT–based quantification of vertebral trabecular parameters in control and *Atpif1*$^{\Delta LysM}$ mice at 6 and 18 months of age. (**h**) Vertebral trabecular number. (**i**) Vertebral trabecular thickness. (**j**) Vertebral trabecular spacing. Data are means ± s.d. Statistical analyses were performed using two-way ANOVA. Exact *P* values are shown in the panels.

Supplementary Fig. 10. Additional *ex vivo* analyses of mature osteoclasts from control and *Atpif1*$^{\Delta LysM}$ mice. (**a, b**) Representative TRAP staining images (**a**) and quantification of TRAP-positive multinucleated cells (MuNCs) per well (**b**) in osteoclast cultures generated from control and *Atpif1*$^{\Delta LysM}$ mice. (**c, d**) Relative mRNA expression of osteoclast marker genes. (**d**) MitoSOX

Red fluorescence intensity per cell in osteoclast cultures from control and *Atpif1*$^{\Delta LysM}$ mice. Data are means ± s.d. Statistical analyses were performed using an unpaired two-tailed Student's t-test. Exact *P* values are shown in the panels. All *ex vivo* measurements were performed in cultured BMMs pooled from 5 mice/group.

Supplementary Fig. 11. Histomorphometric analyses of femoral endocortical bone in aged mice treated with gossypol. From left to right: Number of osteoclasts per bone perimeter (N.Oc/B.Pm). Number of osteoblasts per bone perimeter (N.Ob/B.Pm). Osteoclast surface per bone surface (Oc.S/BS). Osteoclast number relative to osteoclast perimeter (N.Oc/Oc.Pm). (n = 7–9 animals/group). Data are means ± s.d. Statistical analyses were performed using an unpaired two-tailed Student's t-test. Exact *P* values are shown in the panels.